Wind-Tunnel Measurements on Bodies and Wing-Body Combinations

by
D. Althaus
Institut für Aerodynamik und Gasdynamik
der Universität Stuttgart

Introduction

In recent times the wing drag of airplanes has been substantially reduced through use of modern laminar airfoils. A further gain can be achieved by reducing the drag of the fuselage and the interference drag. Experimental investigations have been made in order to show the possible reduction in drag of fuselages and, moreover, to get some idea of the interaction of the fuselage with a wing and the influence of various wing positions. The measurements were made in the Laminar Wind Tunnel of the Institut für Aerodynamik und Gasdynamik der Universität Stuttgart.

Measurement of drag

The drag of the bodies and of wing-body combinations was measured by a pitot rake rotating in steps of 15 degrees around the axis at the end of the body. The rake was 150 mm high. The static pressure in the boundary layer was measured by three static tubes. The total pressure of the 48 rake tubes was measured by one pressure transducer via a scanivalve. The data were punched on cards and evaluated on a digital computer.

The fuselage models were mounted on a sting fixed to the wind tunnel turntables. The models of wing-body combinations were mounted with their wing tips attached to the turntables. Measurement of the drag of wing-body combinations with an external balance proved to be unreliable, owing to the interference of the wing tips with the tunnel boundary layer.

Measurement of lift

The lift of the wing-body combinations was measured by integrating the pressure along the tunnel walls and by an external balance. Both methods gave the same results.
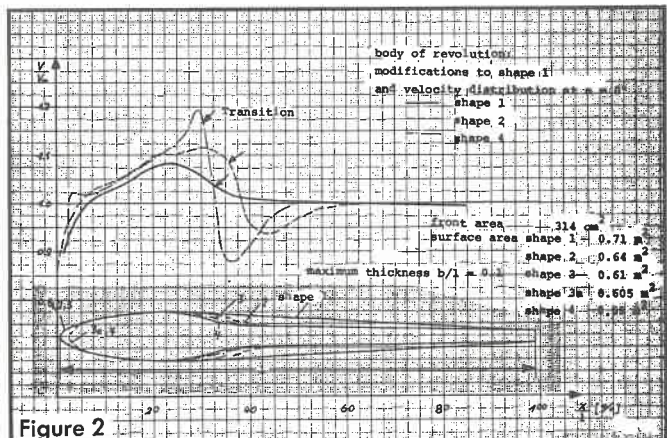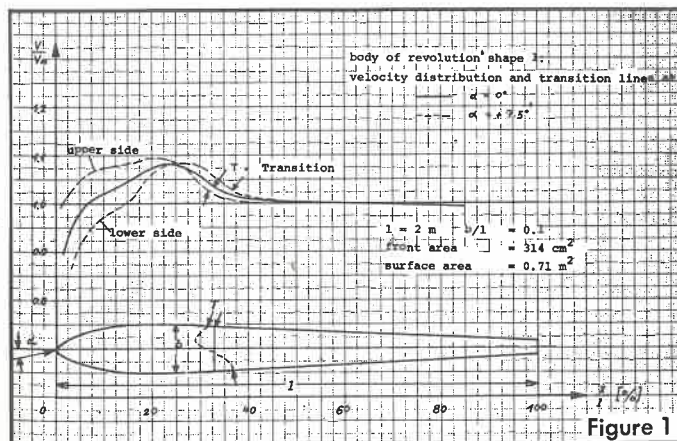
Measurements on fuselages

A fuselage should offer enough volume for the pilot and should have a drag as small as possible. For a given frontal area this can be achieved in two ways:

1. Similar to laminar airfoils, the front part of the body should produce favorable pressure gradients in all meridians even at incidences of about $\pm$ 10 degrees. At the same time the whole surface should be smooth and leak-free in order to avoid any disturbances to the laminar flow.
2. Behind the transition front it is favorable to contract the cross-section. On one hand this reduces the wetted surface, on the other hand it shifts the unavoidable pressure rise to the thinner parts of the turbulent boundary layer, which is a well-known principle of favorable boundary layer control.

In order to investigate different degrees of contraction, measurements were made on a body of revolution with various modifications. In all cases the thickness-to-length ratio was 0.1 at $x/L = 0.25$. The Reynolds number based on body length was $Re = 7.1 \times 10^6$ for all measurements reported, unless otherwise specified. The shape of the base model (shape 1), its pressure distributions, and transition line are illustrated in Fig. 1. At incidence the transition line is only slightly shifted from its position $x/L = 0.33$ at $\alpha = 0$. The rear part of the fuselage is formed by a conical cylinder tangent to the front part at maximum cross section.

Modifications to base shape 1

Shape 1 was modified in the following ways: Three different contraction parts were inserted between the front part and a cone with small diameter, yielding shapes 2, 3, and 4 (Fig. 2). Shape 3 was further modified to shapes 3a and 4 with a blunter nose. The velocity distributions of shapes 1,
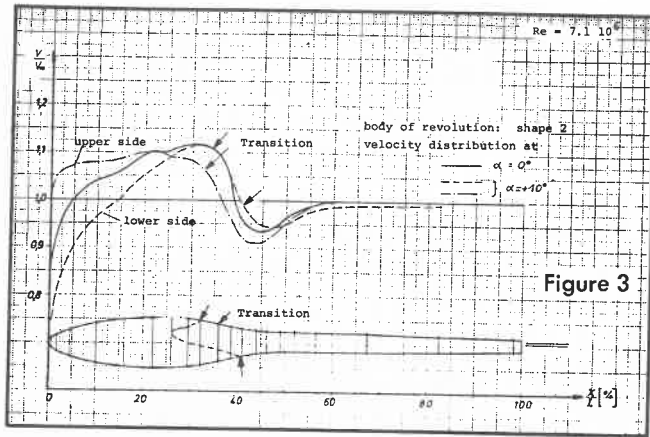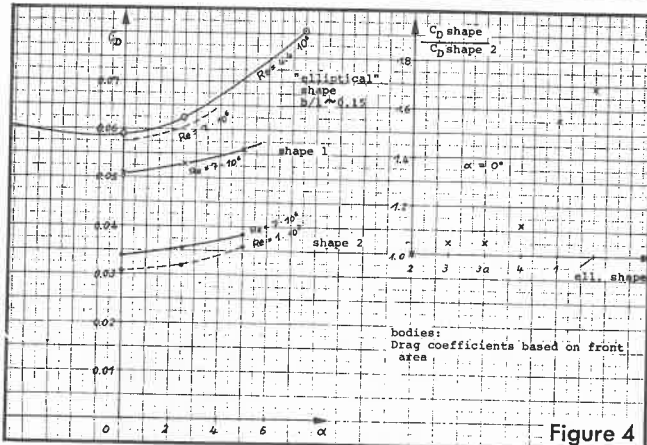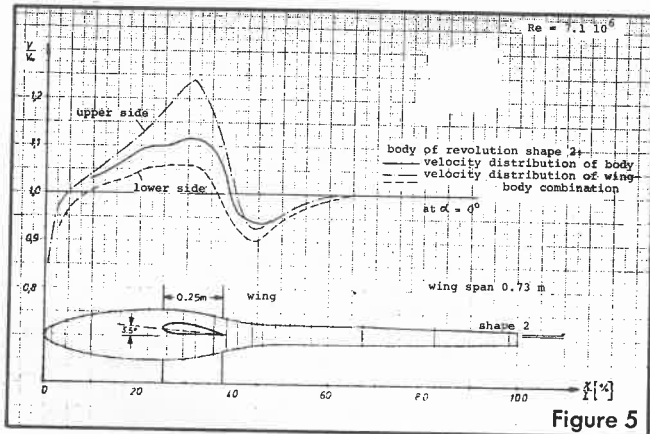

Figure 1

Figure 2

Figure 3

Figure 4

Figure 5

As the influence of incidence is nearly the same for all shapes of the bodies of revolution, the drag coefficients of the other shapes tested are only plotted in relation to the drag coefficients of shape 2 (see right side of Fig. 4, $\alpha = 0$ degrees and Re $= 7 \times 10^6$). The drag coefficients of shapes 3, 3a and 4 with the stronger contractions are higher than those of shape 2 due to the steeper pressure rises in the contraction part and correspondingly earlier transition as demonstrated in Fig. 2. There is no difference in drag between shapes 3 and 3a (up to incidences of $\alpha = \pm 7$ degrees), which differ only in having a sharp or blunt nose. A sharp nose results in only a slight increase of the wetted surface. Shape 2 has the lowest drag of all the shapes tested.

Measurements on wing-body combinations

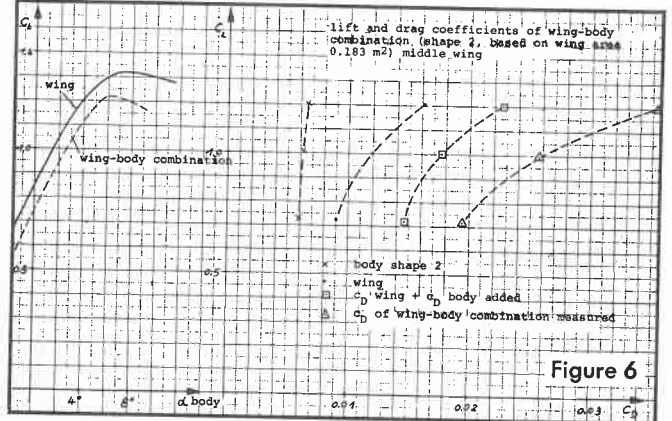Wing-body combinations not only produce complicated pressure distributions at their junction but also lead to a
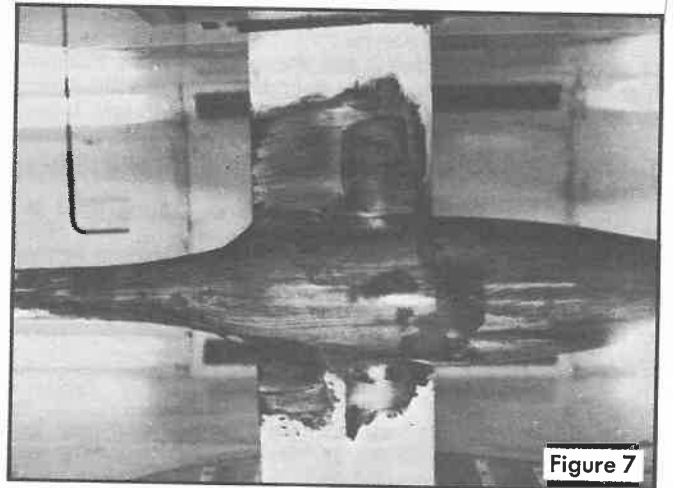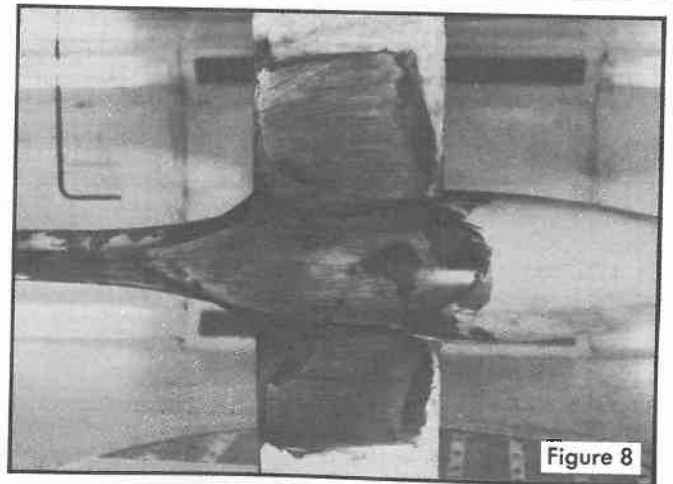

Figure 6

Figure 7

Figure 8

2, and 4 are given in the upper part of Fig. 2. Obviously the position, the maximum value of the velocity peaks, and the total pressure rise correspond to the local surface curvature of the contraction part. The transition lines are influenced in the same way. Fig. 3 shows the variation of velocity distribution and transition lines due to angle of attack, for shape 2.

The left side of Fig. 4 presents the drag coefficients (based on frontal area) versus angle of attack for shapes 1 and 2. There is only a gradual increase of drag with incidence. The transition lines are nearly unchanged, as shown in Fig. 3, but there is a considerable drag reduction from shape 1 to shape 2. The drag of all shapes is lowered further by increase in Reynolds number.

The drag polar labeled as "elliptical shape" in Fig. 4 corresponds to a body which is built up of an ellipsoid in the front part, with a linear continuation to a circular cross-section at its end (idealized body of the sailplane Ka-6). This body is used for examining the influence of various vertical wing positions, as described below.

strong interference with the boundary layers of the wing and the body. To get some experimental results, the body with shape 2 was fitted with a wing as shown in Fig. 5. The wing is in mid-wing position just above the mean line of the body. The wing airfoil has a thickness/chord ratio of 0.18 and spans the tunnel width (0.73 m). The maximum diameter of the body is 0.2 m. The lift and drag coefficients of this wing-body combination, based on wing area, are plotted in Fig. 6. The lift coefficients of the isolated wing are reduced
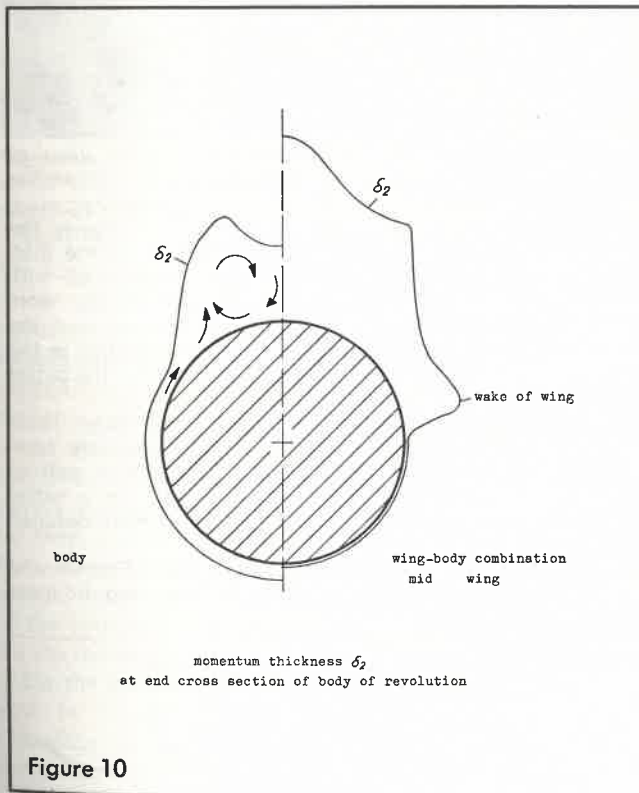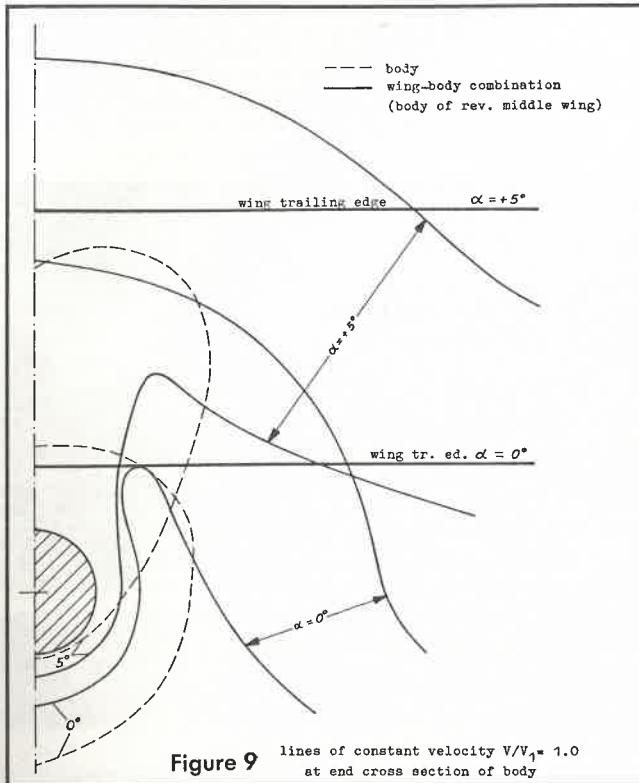
by the interference of the body; the angle of attack corresponding to maximum lift is reduced by about one degree. In the lift-drag polar, the drag of the isolated parts and their arithmetic sum, together with the drag of the wing-body combination, give an indication of the interference drag which increases with increasing lift.

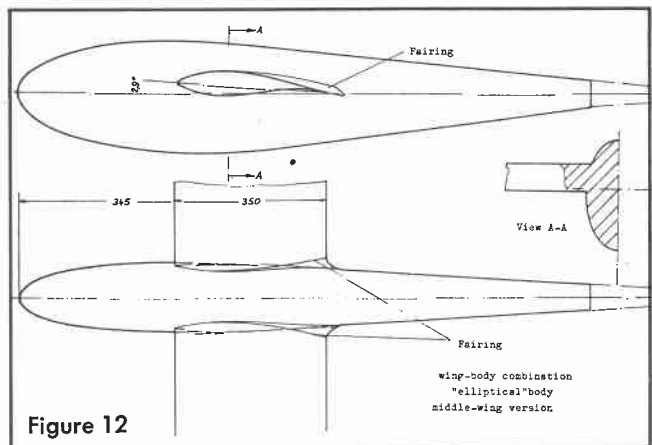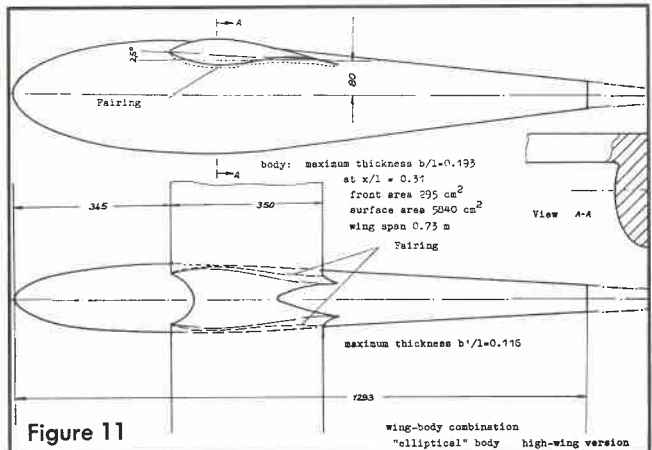In Figs. 7, 8, 9 and 10 some details of the flow are shown:

Fig. 7 is a photograph of the upper side with an oil-film at $\alpha = 0$ degrees incidence, showing the wall streamlines. In Fig. 8 the incidence is increased to 5 degrees, that is, almost to the maximum lift condition. Flow separation appears near the rear part of the wing-body junction with a vortex on each wing, and a distinct divergence and convergence of streamlines on the body above the wing. The fairing on the upper side of the wing-body junction (see Fig. 7) has no influence on the lift characteristics but increases the drag at low incidence approximately five percent.

In Fig. 9, lines of constant velocity $V/V_1 = 1.0$ at the end cross-section of the body are plotted for the isolated body and the wing-body combination. The wake of the wing is raised near the body and seems to continue above the body. The angle of downwash has the same distribution, yielding a decrease in spanwise lift and, accordingly, additional induced drag. On the lower side of the body the thickness of the boundary layer is diminished.

In Fig. 10 the momentum thickness δ_2 is plotted around the circumference of the body end for $\alpha = +5$ degrees incidence. The left side holds for the isolated body and the right side for the combination.

The influence of wing position

To investigate the influence of the vertical position of the wing, the elliptical body (already mentioned) and a wing with a chord of 0.35 m (airfoil t/c = 0.184) were used. The two different versions of the model are shown in Figs. 11 and 12. For the high-wing version a fairing was used at the intersection of the lower wing surface with the body. In

Figure 9   lines of constant velocity $V/V_1 = 1.0$
at end cross section of body

momentum thickness δ_2
at end cross section of body of revolution

Figure 10

Figure 11   wing-body combination
"elliptical" body   high-wing version

Figure 12   wing-body combination
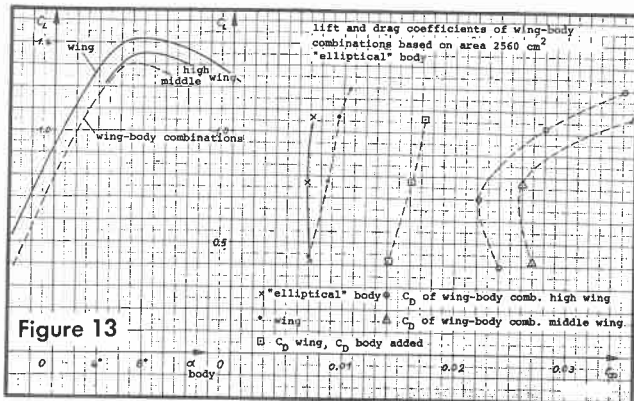"elliptical" body
middle-wing version

Figure 13

this way separation at negative incidences could be delayed by one degree. With the mid-wing version (Fig. 12) no change in lift characteristics could be observed by fairing the upper wing-body intersection, but the drag at low incidence was increased by some five percent.

The lift and drag coefficients (based on wing area) of the two versions and of the isolated parts are plotted in Fig. 13 in the same manner as for the wing-body combination of Fig. 6. There is a distinct difference in lift characteristics: The lift polar of the high-wing version is similar to the polar of the isolated wing (maximum lift at same incidence). On the mid-wing version, separation occurs earlier and the maximum lift is smaller. The drag coefficients of the mid-wing are about 13 percent higher than those of the high-wing version, the difference increasing with higher lift coefficients. The difference between the drag coefficients measured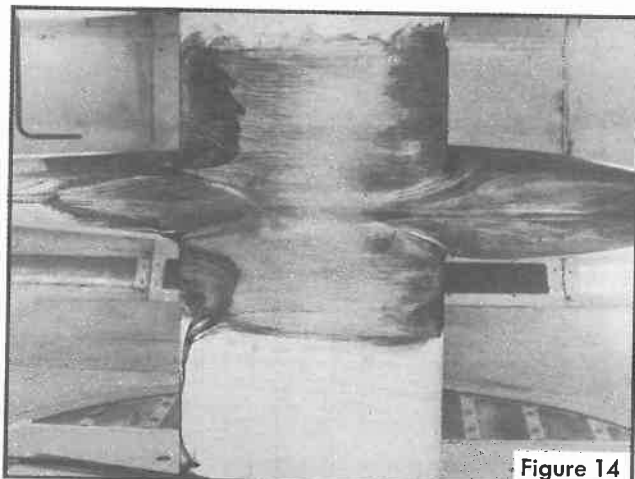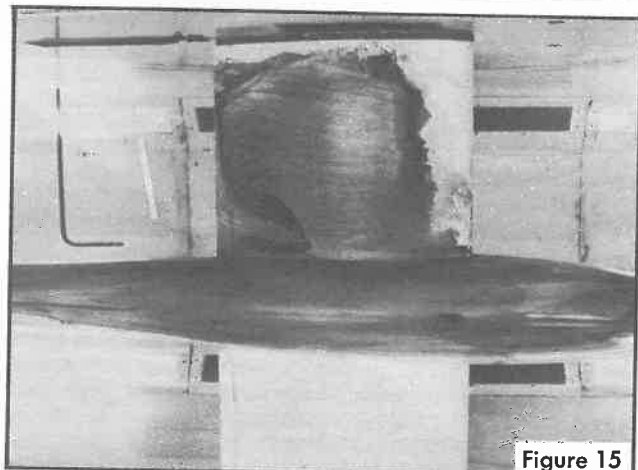 on the wing-body combinations and the drag coefficients composed of the sum of the drag coefficients of the isolated parts is a measure of the interference drag. This difference has a minimum at $\alpha = 0$ degrees incidence of the body.

Photographs of the different models with an oil film help to reveal some details of the flow mechanisms:

Fig. 14 shows the upper side of the high-wing model at $\alpha = +6$ degrees incidence ($C_L = 1.3$). Fig. 15 shows the mid-wing model at $\alpha = +5.5$ degrees ($C_L = 1.25$). Both configurations exhibit a region of separated flow containing two vortices on each wing near the body. On the high-wing model the separation begins further downstream, and the vortices are rather separated from each other, while on the mid-wing model separation begins at nearly half chord of the wing and spreads in a wedge shape over the wing. There is only a small distance between the two vortices and they seem to be more intense.
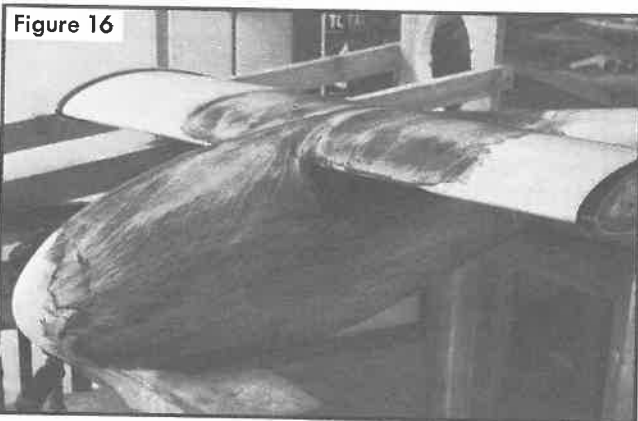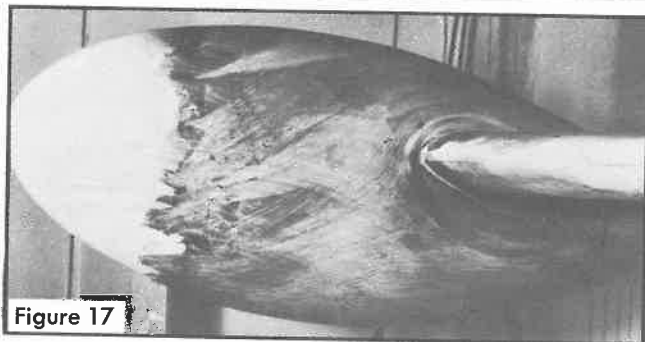

Figure 16

Figure 14

Figure 17

Figure 15

Figs. 16 and 17 show the corresponding side views of the two model configurations, demonstrating the streamline patterns on the front portions. The position of the stagnation points in relation to the wing leading edge is nearly the same on both models. The dividing streamline on the mid-wing model, however, originates much lower than with the high-wing version. In consequence, substantially more boundary-layer material of the forebody is swept over the endangered upper side of the wing-body junction than in the high-wing case. This is undoubtedly one reason for the better performance of the high-wing combination.

The measurements reported here give some rough ideas about the flow mechanism on bodies and wing-body combinations. Since the wing spans completely from wall to wall, the wing flow is mostly two-dimensional. For a better understanding of the complex flows, more and more detailed measurements are required in this area.

I am indebted to Eberhard Schott and Klaus Fischer who built the models, assisted with the experiments, and did most of the evaluation work.